Analysis and Design of Discrete Ferrite Rings to Improve the Efficiency of Meter-Range Wireless Gap Inductive Power Transfer System

Peng Gu, *Member, IEEE*, Dongsheng Yang, *Senior Member, IEEE*, Guangdi Li, *Member, IEEE*, Bowen Zhou, *Member, IEEE*, Fang Wei, *Member, IEEE*, and Honglu Guan

***Abstract*—In this article, discrete Ferrite rings (DFRs) applied to cylindrical solenoid coupler (CSC) is proposed. The coupling coefficient between adjacent coils is enhanced and the inductance of the coils is increased by reducing the reluctance in the magnetic circuit. The DFRs-based CSCs magnetic structure is considered to be applied for post insulators. The inductive power transfer (IPT) system based on the abovementioned magnetic structure is used to power the state detection equipment at high potential points. A finite element simulation analysis of the electric field is finished to verify that the addition of DFRs does not affect the insulation properties of the post insulator. The parameters of DFRs are optimized to improve their effect on coupling coefficient and self-inductance based on the finite element method. The multilayer coils and the decoupling series compensation method are analyzed. The circuit model of the three-stage IPT system is built and analyzed. A 1.54 m long-range IPT system prototype is completed to simulate the 110 kV post insulator. A series of experiments are performed to verify the advantages of the proposed DFRs. Efficiency of the meter-range IPT system can reach 75.4%.**

***Index Terms*—Discrete ferrite rings, efficiency optimization, inductive power transfer, magnetic coupling structure design, smart grid applications.**

I. Introduction

With the development of inductive power transfer technology, more diversified application scenarios have been developed in recent years. Applications in novel fields such as unmanned transportation electrification (unmanned aerial vehicles and autonomous underwater vehicles), wireless motors, and smart grids have been gradually discovered. For different scenarios, it is necessary to design corresponding magnetic coupling structures to realize wireless power transfer (WPT) according to relevant requirements [1], [2], [3], [4], [5].

Among them, the exploration of inductive power transfer system design to extend the wireless distance is particularly challenging. Quality factor and coupling coefficient are the key factors to improve the efficiency of wide wireless gap inductive power transfer (IPT) system [6], [7], [8].

Recent references have improved the efficiency of the system by increasing the quality factor of the coupler. Generally, reducing the resistance and increasing the frequency are effective ways. Litz-wire square solenoid coils were proposed in [9]. By analyzing the influence factors such as skin effect and proximity effect, the corresponding frequency corresponding to the optimal quality factor is obtained, and the efficiency of the IPT system is improved. A cylindrical high-frequency wireless power transfer magnetic coupling structure was proposed in [10], and a strong misalignment tolerance WPT efficiency of about 70% at a frequency of 27.12 MHz was achieved under a wide gap. In [11], a single-turn air-core copper coil by advanced three-dimensional casting method is obtained, and wide gap WPT at 6.78 MHz and 13.56 MHz was realized. Among them, more space is needed to overcome the proximity effect and skin effect. Besides, the cost of MHz high-frequency converters is expensive.

In addition, the enhancement of the coupling coefficient is also an important method to improve the efficiency of the wide gap IPT systems. In [12], [13], and [14], scholars proposed a dipole-shaped magnetic coupling structure applied to meter-range wireless gap IPT systems. Methods including core layout optimization, comparative analysis of primary and secondary magnetizing inductance and optimal ampere-turn design have been proposed to optimize the efficiency characteristics of the IPT system. The demagnetizing factors of a cylindrical ferrite core and a novel ferrite core were investigated in [15]. A free arrangement IPT system with a ferrite transmission medium to extend the distance was proposed in [16]. A cubic magnetic coupler based on ferrite core longitudinal split method was proposed in [17], the coupling coefficient is improved at the same distance-to-diameter ratio. The analysis and design of the abovementioned couplers are based on the ferrite material

Manuscript received 20 March 2023; revised 26 May 2023; accepted 13 June 2023. Date of publication 28 June 2023; date of current version 1 September 2023. This work was supported in part by the Joint Funds of the National Natural Science Foundation of China: Self-organizing Aggregation and Regulation Theory of Massive Resources Virtual Power Plant for Power Grid Balance Demand under Grant U22B20115, and in part by the Fundamental Research Funds for the Central Universities under Grant N232405-27. Recommended for publication by Associate Editor F. Lu. *(Corresponding authors: Dongsheng Yang; Fang Wei.)*

Peng Gu, Dongsheng Yang, Guangdi Li, and Bowen Zhou are with the College of Information Science and Engineering, Northeastern University, Shenyang 110819, China (e-mail: gupeng@mail.neu.edu.cn; yangdongsheng@mail.neu.edu.cn; liguangdi@mail.neu.edu.cn; zhoubowen@ise.neu.edu.cn).

Fang Wei is with the Institute of Foreign Languages, China Medical University, Shenyang 110122, China (e-mail: fwei@cmu.edu.cn).

Honglu Guan is with the State Grid Henan Electric Power Research Institute, Zhengzhou 450000, China (e-mail: 1909899842@qq.com).

Color versions of one or more figures in this article are available at https://doi.org/10.1109/TPEL.2023.3288302.

Digital Object Identifier 10.1109/TPEL.2023.3288302

with high magnetic permeability characteristics. Efficiency of wide gap IPT systems is improved through improved coupling coefficient.

In the case of powering smart grid sensors, meter-range wireless gaps are necessary. Since the wireless gap between the two stages is further extended, the efficiency of the system is reduced to a very low level. Therefore, IPT systems with domino architecture formed by relay coils were proposed and analyzed in [18], [19], and [20].

In recent years, relevant references have focused on the applications of meter-range wireless gap IPT technology in smart grid for 110 kV high voltage insulation distance. A two-coil structure applied to 110 kV insulator strings was proposed in [21]. Due to the low coupling coefficient, efficiency of the systems is not high. A solution to harvest power from the magnetic field around a 110 kV transmission line was proposed in [22], which magnetic field required for its power transfer bypasses the insulating device. A method of realizing constant voltage/constant current mode by switching the system mode for battery charging was proposed in [23]. The IPT systems based on PCB self-resonant magnetic coupling structure to achieve better consistency for each stage was proposed in [24] and [25].

A three-stage IPT system based on cylindrical solenoid coupler (CSC) applied for 110 kV post insulators was proposed in [26], 59.5% efficiency was achieved. In order to further extend the wireless gap to match the insulation distance of higher voltage levels, efficiency of the IPT system needs to be further improved. This article is a continuation of [26]. The efficiency is expected to be improved by increasing the quality factor and coupling coefficient of CSC.

The rest of this article is organized as follows. Discrete ferrite rings are proposed and designed in Section II. The circuit model of the decoupling distributed compensation and the output characteristics of the IPT system are analyzed in Section III. In Section IV, a prototype simulating the length of a 110 kV post insulator is built and the experimental results are analyzed. Finally, Section V concludes this article.

II. Analysis and Design of the Discrete Ferrite Rings

A. Key Factors for Long-Range IPT System Efficiency

For a basic two-stage inductive power transfer system, and the losses of the converters are ignored. Assuming that the primary and secondary sides of the IPT system based on S/S series compensation are symmetrical. Therefore, the maximum power transfer efficiency equation of IPT system could be expressed as [8]

$$\eta_{\max}=\frac{k^2Q^2}{\left(1+\sqrt{1+k^2Q^2}\right)^2}. \tag{1}$$

The coupling coefficient k and the quality factor Q together determine the maximum efficiency of the coil–coil part of IPT system from the above equation. For wide gap IPT systems, more magnetic flux is leaked into air, the value of coupling coefficient k is usually less than 0.1. The contour map corresponding to (1) under low coupling coefficient with quality factor Q varies from 100 to 3000 is obtained in Fig. 1, which abscissa takes the logarithm to reflect the changing trend of the coupling coefficient under the condition of wide gap.

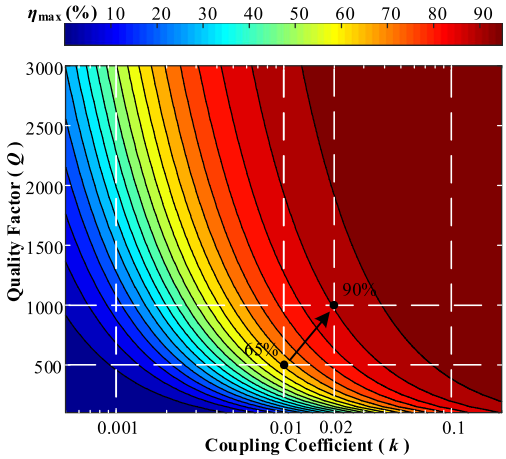

Fig. 1. Maximum efficiency of IPT systems under low coupling coefficient.

It can be found in the abovementioned figure that the coupling coefficient plays a decisive role in the maximum efficiency of the wide air gap IPT system. When the coupling coefficient is greater than 0.1, even if the quality factor of the coil is less than 500, the maximum efficiency can still easily reach more than 90%, which is usually the case for narrow air gap IPT systems. When the coupling coefficient is between 0.01 and 0.1, the quality factor is preferably higher than 500 to make the highest coil–coil efficiency reach a higher level. When the coupling coefficient is between 0.001 and 0.01, even if the quality factor is higher than 2000, it is difficult to ensure that the efficiency is greater than 80%. Finally, when the coupling coefficient is less than 0.001, the efficiency will not be too high unless a high-quality coil with a quality factor higher than 3000 is used, which will greatly increase the cost of the system. To give a simple example, if the coupling coefficient is increased from 0.01 to 0.02, and the quality factor is increased from 500 to 1000, then the maximum efficiency of the system can be drastically increased from 65% to 90%, as shown in Fig. 1.

Therefore, as $Q=\omega L/R=2\pi fL/R$, the quality factor Q can be increased by increasing inductance value L, reducing resistance value R or increasing the frequency f of the system. Importantly, improving the coupling coefficient k by optimizing the design of the coupler is an effective way to improve the efficiency of wide gap IPT.

In [26], an IPT system with a 1 m-length wireless gap based on three-stage CSC is proposed. The system can supply power for state detection equipment at high potential points by means of a 110 kV high voltage post insulator with a 59% efficiency. However, in order to further extend the distance of wireless power transfer and supply power to condition monitoring equipment at a voltage level higher than 110 kV. It is necessary to further improve the system efficiency to meet the above requirements.

In this way, discrete Ferrite rings (DFRs), as shown in Fig. 2, are proposed, in this article, to improve the coupling coefficient and inductance value of CSC. The proposed DFRs would

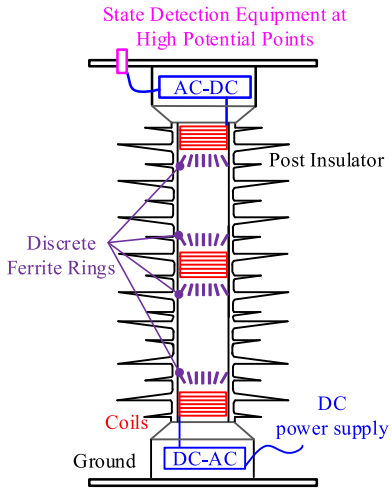

Fig. 2. Application scenarios of DFRs.

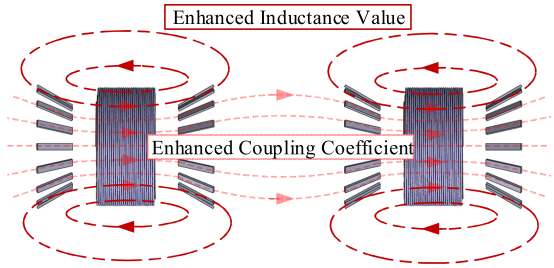

Fig. 3. Analysis of DFRs for enhancing inductance value and improving coupling coefficient.

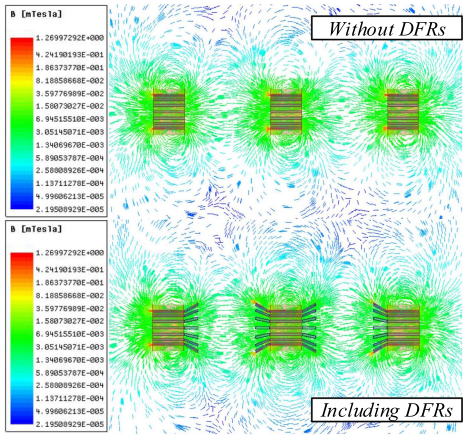

Fig. 4. Finite element simulation analysis of magnetic field under the same excitation.

further improve the efficiency of inductive power transfer system under large wireless gap for high voltage equipment condition monitors power supply applications.

B. Analysis of Discrete Ferrite Rings

The basic principle of DFRs to improve the efficiency of large wireless gap IPT is to rebuild the magnetic circuit of the magnetic coupling structure. The magnetic permeability of the ferrite core is much greater than that of air, and forms a strong pooling effect on the leaked magnetic flux.

Take the magnetic coupling structure with the same primary and secondary sides as an example. Equation (2) is Ohm's law in a magnetic circuit. The relationship between inductance and flux is described in (3) as follows:

$$\phi R_{\mathrm{m}} = NI \tag{2}$$

$$LI = N\phi. \tag{3}$$

Therefore, the relationship between self and mutual inductance and reluctance is obtained in

$$\begin{cases} L \propto \frac{1}{R_{\mathrm{m\_L}}} \\ M = k\sqrt{L_{\mathrm{P}} L_{\mathrm{S}}} = kL \propto \frac{1}{R_{\mathrm{m\_M}}}. \end{cases} \tag{4}$$

Among them, in the magnetic circuit with the same primary and secondary sides, $R_{\mathrm{m\_L}}$ is the sum of the reluctance associated with all the magnetic fluxes generated by the magnetomotive force excited by the primary or secondary coil. $R_{\mathrm{m\_M}}$ is the sum of the reluctance associated with the magnetic flux linked by the original and secondary coils exciting the magnetomotive force. The addition of DFRs simultaneously reduces both $R_{\mathrm{m\_L}}$ and $R_{\mathrm{m\_M}}$ according to the magnetic flux distribution characteristics of CSC. Therefore, in a two-stage magnetic coupling structure, as shown in Fig. 3, DFRs provide a low reluctance path for magnetic flux.

Among them, the discrete shape reduces the use of ferrite cores, the weight and cost are cut down. The angle of inclination guides the direction of the magnetic field lines. In this way, the self-inductance and mutual inductance value of the magnetic coupling structure is increased and the coupling coefficient is strengthened. In order to preliminarily verify the abovementioned conclusions, the finite element analysis (FEA) model is established. The finite element simulation analysis of the magnetic field under the same excitation is completed, as shown in Fig. 4. Compared with the case of without DFRs, the magnetic flux around the coils is significantly enhanced, and the flux linkage interaction between adjacent couplers is more obvious in figure Including DFRs.

In order to verify that the inclusion of DFRs will not affect the electric field distribution of the original system, and will not damage the insulation characteristics of the 110 kV high-voltage post insulator, the finite field analysis model of element electric is established in Fig. 5.

Among them, the voltage between the two electrodes is selected to be 110 kV peak value, which is 155.6 kV. Compared with the case of without DFRs, the enhancement of the electric field distribution is extremely weak in the case of including DFRs. Besides, the strongest value of the electric field in the two groups of finite element simulation analysis results is 1.547×10^6 V/m, which is far lower than the threshold value 3×10^6 V/m for the air to be broken down in the conventional state. The essence of the above phenomenon is that the Mn-Zn ferrite made into the magnetic core is a metal oxide ceramic material, which is a kind of insulating material. Therefore, the inclusion of DFRs does not significantly affect the electric field

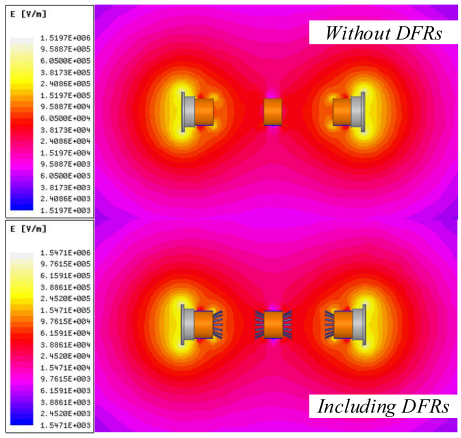

Fig. 5. Electric field distribution at 155.6 kV by finite element method.

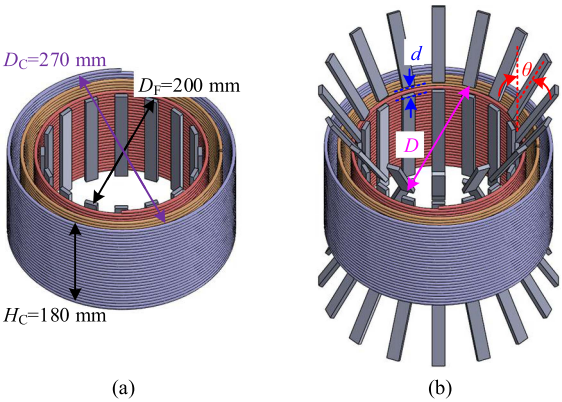

Fig. 6. Details and parameters of CSC and DFRs. (a) Three-layer CSC. (b) CSC based on DFRs.

distribution of the previous system consisting of IPT module and post insulator, and also will not cause obvious discharge phenomenon of the post insulator.

C. Design and Optimization of Discrete Ferrite Rings

In this section, parameters of the proposed DFRs are optimized for their performance in promoting the efficiency of the IPT system. Among them, based on the performance of the litz coil of the three-layer CSC, the improvement effect of DFRs on the self-inductance, mutual inductance and coupling coefficient under different parameters is investigated, as shown in Fig. 6.

The parameters of CSC are designed, among which the coil height H_C is 180 mm, the diameter D_C is 270 mm, and the equivalent diameter of the ferrite core of CSC D_F is 200 mm. In the case of the same amount of ferrite cores, three parameters of DFRs can be optimized. The equivalent diameter D of the DFRs, the inclination angle θ of the DFRs, and the distance d between the DFRs and the CSC coil. Besides, the size of each DFR is $90 \times 15 \times 5$ mm^3. The abovementioned parameters and the intervals that can be optimized are shown in Table I.

A two-stage finite element analysis model of the magnetic coupling structure with 0.5 m wireless gap is established to

TABLE I
PARAMETERS OF DFRS-BASED CSC

Parameter	Value	Parameter	Value
H_C	180 mm	D	100 to 300 mm
D_C	270 mm	θ	0 to 60°
D_F	200 mm	d	0 to 50 mm
Turns n	84	Each *DFR*	90×15×5 mm^3

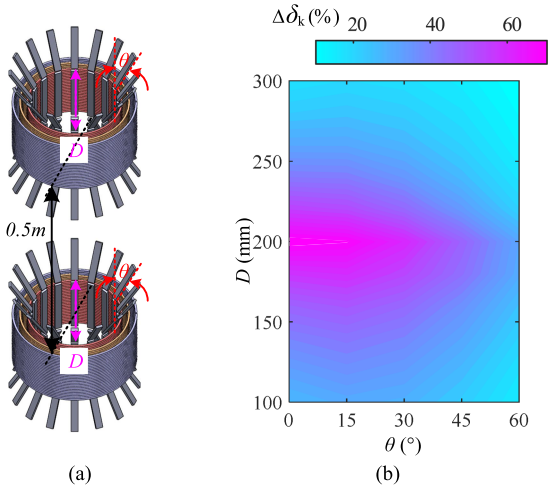

Fig. 7. Two-stage magnetic coupling structure and the influence of parameters on the coupling coefficient. (a) Magnetic coupling structure. (b) The effect on coupling coefficient.

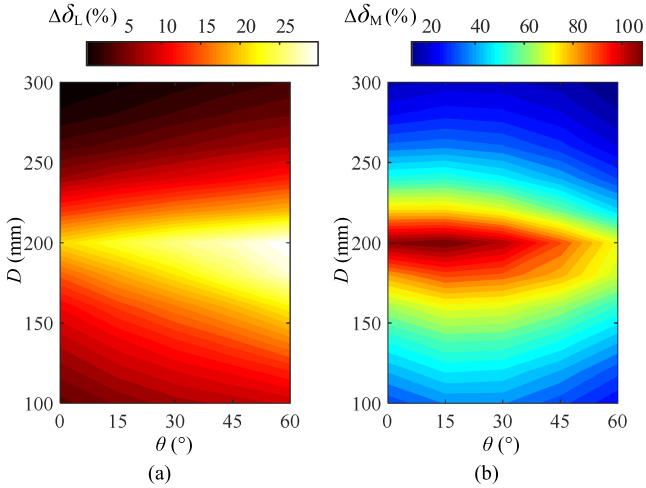

Fig. 8. Effect of D and θ on self-inductance and mutual inductance. (a) The effect on self-inductance. (b) The effect on mutual inductance.

investigate the influence of the changes of the abovementioned parameters on the self-inductance, mutual inductance and coupling coefficient of the coupler.

The changes of D and θ and their influence on the coupling coefficient between two stages are shown in Fig. 7. In addition, the influence of the abovementioned parameters on self-inductance and mutual inductance is shown in Fig. 8.

Among them, the $\Delta\delta_k$, $\Delta\delta_L$, and $\Delta\delta_M$ are respectively the growth rate of the coupling coefficient, self-inductance, and

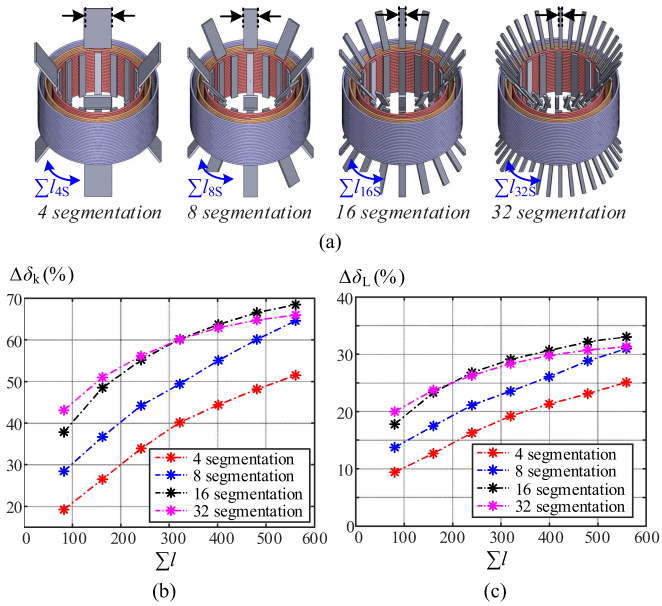

Fig. 9. Analysis of various spacing arrangements between the ferrite cores. (a) 4, 8, 16, 32 segmentation states. (b) Effect on coupling coefficient. (c) Effect on self-inductance value.

mutual inductance compared to the coupling structure without DFRs

$$\Delta\delta_{\mathrm{k}} = 100\% \times \frac{k_{\mathrm{DFR}} - k_0}{k_0} \tag{5a}$$

$$\Delta\delta_{\mathrm{L}} = 100\% \times \frac{L_{\mathrm{DFR}} - L_0}{L_0} \tag{5b}$$

$$\Delta\delta_{\mathrm{M}} = 100\% \times \frac{M_{\mathrm{DFR}} - M_0}{M_0}. \tag{5c}$$

Taking the k_0, L_0, and M_0 in two-stage model based on CSC of Fig. 6(a) as the benchmark value.

In Fig. 7, when the diameter of DFRs is 200 mm, the coupling coefficient increases best. At this time, the magnetic cores of DFRs and the magnetic cores of CSC are in the aligned position. In addition, the coupling coefficient increases most when the inclination angle is less than 30°. Here, the coupling coefficient can be increased by more than 60% at most.

In Fig. 8, the self-inductance and mutual inductance increase effect is the best when the D is 200 mm as in Fig. 7. In addition, the self-inductance grows faster when θ is larger than 15°. Therefore, D is designed to be 200 mm, and θ is designed to be in the range of 15° to 30°, which can make the coupling coefficient, self-inductance, and mutual inductance reach a relatively high level.

The degree of separation and the usage number of ferrites within the ring need to be considered. Therefore, it is necessary to analyze the influence of various spacing arrangements between the ferrite cores on the coupling coefficient and self-inductance value in the coils. The finite element analysis is finished, as shown in Fig. 9. Among them, the separation state of the ferrites is shown in Fig. 9(a). The ferrite core is divided into 4 segmentations, 8 segmentations, 16 segmentations, and

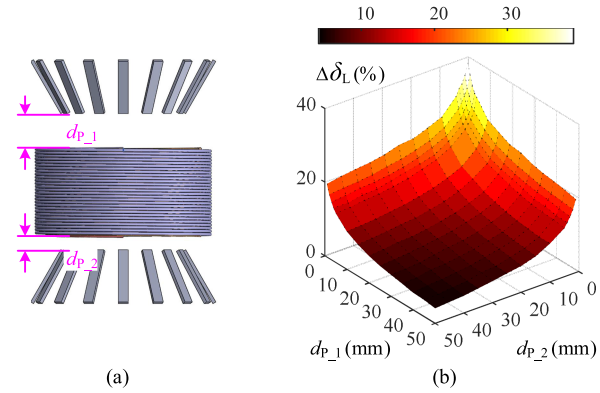

Fig. 10. Effect of d on self-inductance. (a) Magnetic coupling structure. (b) The effect on self-inductance.

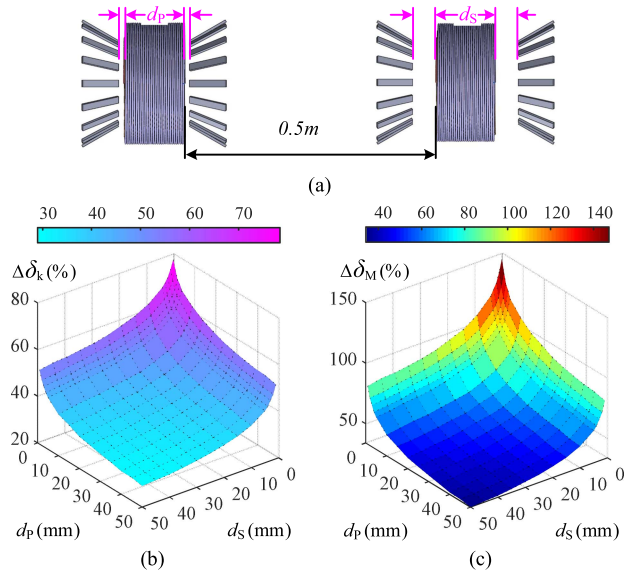

Fig. 11. Effect of d on mutual inductance and coupling coefficient. (a) Magnetic coupling structure. (b) The effect on coupling coefficient. (c) The effect on mutual inductance.

32 segmentations, and the total core consumption is $\Sigma l_{4\mathrm{S}}$, $\Sigma l_{8\mathrm{S}}$, $\Sigma l_{16\mathrm{S}}$ and $\Sigma l_{32\mathrm{S}}$.

The influence on the coupling coefficient and self-inductance value in different segmentation situations changes with Σl is shown in Fig. 9(b) and (c). The tendency of coupling coefficient k and self-inductance value L affected by Σl is similar. As the amount of magnetic core increases, both $\Delta\delta_{\mathrm{k}}$ and $\Delta\delta_{\mathrm{L}}$ show a positive correlation trend, and the growth rate gradually weakens. In the case of the same amount of magnetic core, usually the more times of separation, the more $\Delta\delta_{\mathrm{k}}$ and $\Delta\delta_{\mathrm{L}}$ grow. However, in the states of 16 segmentations and 32 segmentations, the effect may be worse with the amount of magnetic core reaches a certain level with more divisions.

Next, the effect for the position d of DFRs on k, L and M is analyzed in Figs. 10 and 11.

A single DFRs-based CSC is selected and modeled to analyze the effect of its flanking DFRs on self-inductance in Fig. 10. When the DFRs are close to the CSC, the self-inductance $\Delta\delta_{\mathrm{L}}$

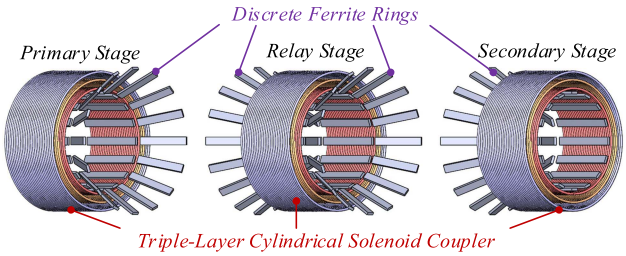

Fig. 12. Meter-range three-stage inductive power transfer system based on DFRs.

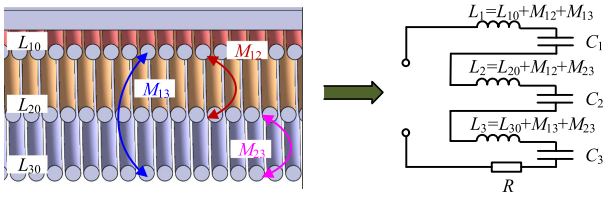

Fig. 13. Decoupled equivalent coil and its compensation capacitors.

can increase by nearly 40%. The abovementioned conclusions can be more obvious in Fig. 11, the coupling coefficient $\Delta\delta_{\mathrm{k}}$ can increase by 80%, and the growth rate of mutual inductance $\Delta\delta_{\mathrm{M}}$ can even be close to 150%.

Therefore, the parameter design and optimization results of CSC based on DFRs can be obtained. Among them, the equivalent diameter D of DFRs needs to be designed to face the ferrite core of CSC. In addition, DFRs need to have a certain angle θ of inclination in the vertical direction. When this inclination angle is designed to be 15° to 30°, the growth of self-inductance and coupling coefficient can be taken into account. Finally, the DFRs should be close to the CSC, the closer they are, the more significant the enhancement effect on the coupling coefficient, self-inductance, and mutual inductance.

III. Decoupled Series Compensation Topology and Circuit Model of the Three-Stage IPT System

A meter-range three-stage inductive power transfer system based on the design of the abovementioned magnetic coupling structure is proposed, as shown in Fig. 12. Among them, the primary side and secondary side are based on single-sided DFRs according to the actual application of post insulator shown in Fig. 2.

In order to achieve high efficiency of wireless power transfer, reactive power compensation of inductive couplers through circuit topology is necessary. Due to the mutual coupling mutual inductance between the layers of the three-layer coil, it is necessary to perform decoupling equivalent for each stage coupler, as shown in Fig. 13.

Among them, the self-inductance of each layer in a single CSC is L_{10}, L_{20}, L_{30}, respectively, and the mutual inductance between any two layers is M_{12}, M_{23}, M_{13}, respectively. Therefore, the equivalent self-inductance of each layer is L_1, L_2, L_3

$$L_1 = L_{10} + M_{12} + M_{13} \tag{6a}$$

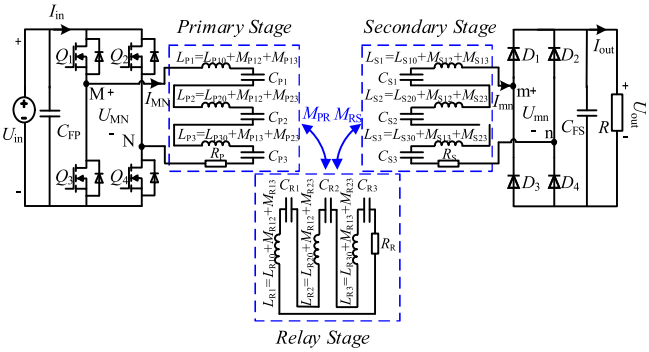

Fig. 14. Circuit model of the three-stage IPT system.

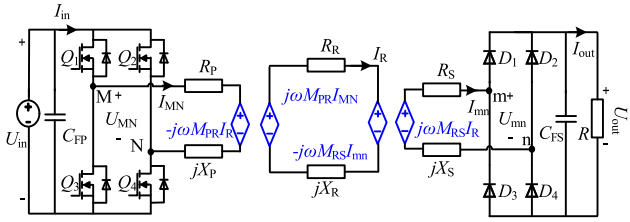

Fig. 15. Simplified circuit model.

$$L_2 = L_{20} + M_{12} + M_{23} \tag{6b}$$

$$L_3 = L_{30} + M_{13} + M_{23}. \tag{6c}$$

In addition, the L_1, L_2, L_3 are compensated by series capacitors C_1, C_2, C_3.

According to the abovementioned analysis, the proposed three-stage IPT system can be constructed as the following circuit model, as shown in Fig. 14.

The system consists of the primary stage, the relay stage, and the secondary stage, and each stage adopts the series compensation method after decoupling equivalent, as shown in Fig. 13. Considering each stage as a whole, the mutual inductance between primary-relay and relay-secondary stages is represented by M_{PR} and M_{RS}. In addition, R_{P}, R_{R}, and R_{S} represent the equivalent series resistance (ESR) in the tertiary circuits.

In view of the complexity of the abovementioned circuit structure, it is simplified to the circuit in Fig. 15. The coupling between two adjacent stages is represented by a controlled source. In addition, the complex inductance and capacitance within each stage is expressed in the form of reactance

$$X_{\mathrm{n}} = j\sum_{i=1,2,3}\omega L_{\mathrm{ni}} - j\sum_{i=1,2,3}\frac{1}{\omega C_{\mathrm{ni}}},\ \mathrm{n} = \mathrm{P},\mathrm{R},\mathrm{S}. \tag{7}$$

Therefore, the circuit can be described by the following system of equations:

$$\begin{cases} U_{\mathrm{MN}} = I_{\mathrm{MN}}R_{\mathrm{P}} - j\omega M_{\mathrm{PR}}I_{\mathrm{R}} + I_{\mathrm{MN}}X_{\mathrm{P}} \\ j\omega M_{\mathrm{PR}}I_{\mathrm{MN}} = I_{\mathrm{R}}R_{\mathrm{R}} - j\omega M_{\mathrm{RS}}I_{\mathrm{mn}} + I_{\mathrm{R}}X_{\mathrm{R}} \\ j\omega M_{\mathrm{RS}}I_{\mathrm{R}} = I_{\mathrm{mn}}R_{\mathrm{S}} + U_{\mathrm{mn}} + I_{\mathrm{mn}}X_{\mathrm{S}}. \end{cases} \tag{8}$$

In a resonant network with the fundamental is considered uniquely, the abovementioned parameters satisfy the relationship as follows:

$$C_{\mathrm{ni}} = \frac{1}{\omega^2 L_{\mathrm{ni}}},\ n = \mathrm{P}, \mathrm{R}, \mathrm{S},\ \ i = 1, 2, 3. \tag{9}$$

Therefore, the inductive and capacitive parts of the reactance completely cancel each other, and there is a relationship of $X_{\mathrm{P}} = X_{\mathrm{R}} = X_{\mathrm{S}} = 0$. Therefore, the output voltage can be obtained in (10). Among them, the equivalent resistance R_{eq} between m and n is represented by $R_{\mathrm{eq}} = 8R/\pi^2$

$$U_{\mathrm{out}} = \frac{U_{\mathrm{in}}\omega^2 M_{\mathrm{PR}} M_{\mathrm{RS}} R_{\mathrm{eq}}}{\omega^2 M_{\mathrm{RS}}^2 R_{\mathrm{P}} + \omega^2 M_{\mathrm{PR}}^2 R_{\mathrm{S}} + \omega^2 M_{\mathrm{PR}}^2 R_{\mathrm{eq}} + R_{\mathrm{P}} R_{\mathrm{R}} R_{\mathrm{S}} + R_{\mathrm{P}} R_{\mathrm{R}} R_{\mathrm{eq}}}. \tag{10}$$

Generally, for the case where the ESR can be neglected $R_{\mathrm{P}} = R_{\mathrm{R}} = R_{\mathrm{S}} = 0$. Therefore, the voltage ratio of the IPT system is $G = U_{\mathrm{out}}/U_{\mathrm{in}} = M_{\mathrm{RS}}/M_{\mathrm{PR}}$. The IPT system can be viewed as a voltage source that can achieve a constant voltage output. However, in the proposed system, the number of turns of the coil reaches 84 turns, so its ESR value is large and cannot be ignored. The abovementioned situation will cause the output voltage of the system to fluctuate with the load change.

IV. Experimental Verification

A. Two-Stage IPT System Tests

A two-stage cylindrical solenoid coupler prototype based on discrete ferrite rings is completed, and the parameters are shown in Table I. Among them, the equivalent diameter D of DFRs is selected as 200 mm, the outer edge of the magnetic ring is aligned with the outer side of the coil, and the inclination angle θ is 25°.

In addition, taking the two-stage prototype based on CSC in Fig. 6(a) as the reference value, the measurement results of the self-inductance and coupling coefficient of the coupler based on DFRs changing with the position of DFRs d are shown in Fig. 16. In the figure, the experimental method refers to Figs. 10 and 11, and the experimental results are compared with the abovementioned two figures. Besides, the FEA results in Figs. 10(b) and 11(b) are shown by dotted lines in Fig. 16. Among them, the test results are in the same trend as the dotted line data obtained by FEA, and the previous analysis is verified.

Therefore, in the design of the coupler, the DFRs are infinitely close to the CSC, and $d_{\mathrm{P}} = d_{\mathrm{P\_1}} = d_{\mathrm{P\_2}}$, $d_{\mathrm{S}} = d_{\mathrm{S\_1}} = d_{\mathrm{S\_2}}$, $d_{\mathrm{P}} = d_{\mathrm{S}}$ are designed as 3 mm in the coupler prototype.

A two-stage IPT system prototype is built to initially verify the effect of DFRs on the efficiency improvement of inductive power transfer, as shown in Fig. 17. Among them, whether to include DFRs is the difference between two groups of controlled experiments.

A series of tests based on the above system were performed, as shown in Fig. 18. The load resistance value changes from 20 Ω to 200 Ω, the maximum efficiency of the system without DFRs is 73.87%, and the maximum efficiency of the system including DFRs is 80.67%.

The power, efficiency, and waveform situations at the two maximum efficiency points are shown in Fig. 19. Among them, the addition of DFRs increased the maximum efficiency of the two-stage IPT system by about 7%. In addition, the abovementioned tests are all finished in the state of system resonance, as shown in the waveform figures.

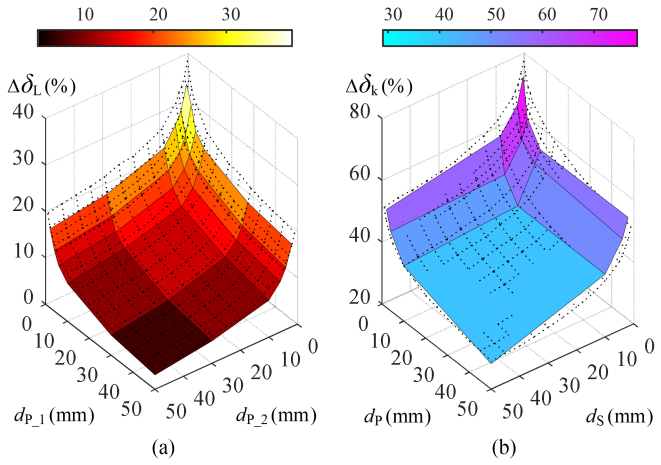

Fig. 16. d affects the test results of coupler self-inductance and coupling coefficient and the comparison with simulation analysis. (a) The effect on self-inductance. (b) The effect on coupling coefficient.

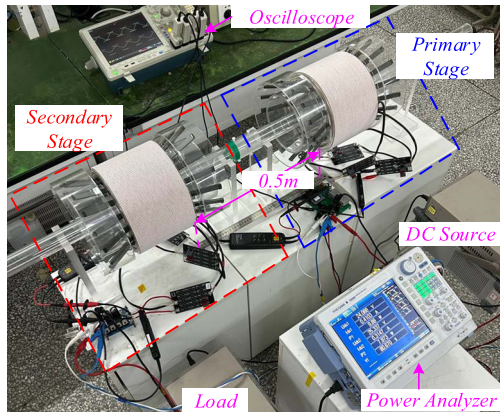

Fig. 17. Two-stage IPT system prototype.

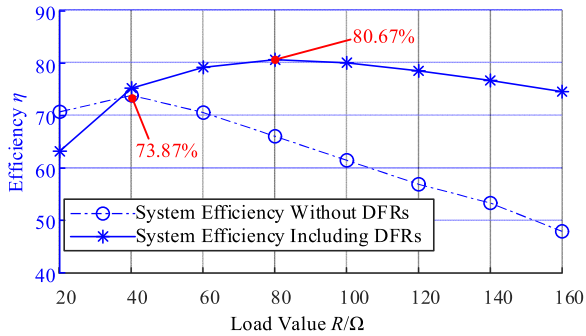

Fig. 18. Efficiency curves of the IPT system.

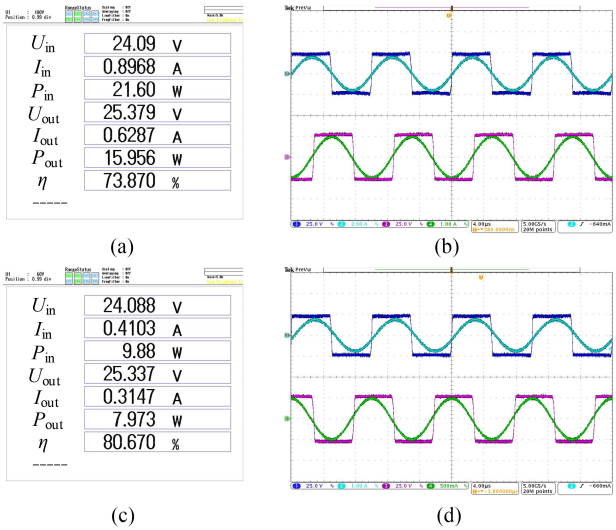

Fig. 19. Power, efficiency, and waveforms of the IPT system under the maximum efficiency of the two group tests. (a) Maximum system efficiency without DFRs. (b) Waveforms of the AC sides under the maximum efficiency point without DFRs. (c) Maximum system efficiency including DFRs. (d) Waveforms of the AC sides under the maximum efficiency point including DFRs.

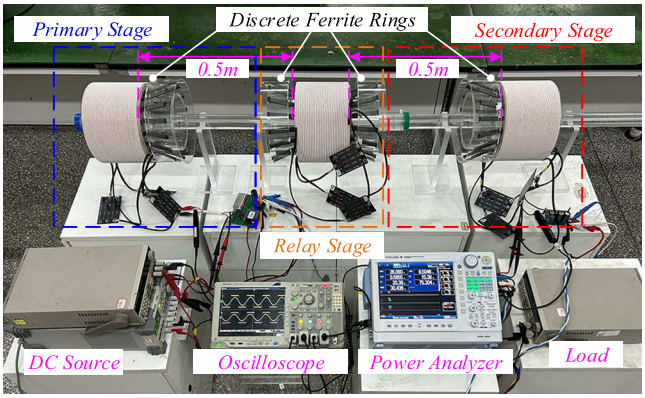

Fig. 20. Prototype of the three-stage meter-range IPT system.

B. Three-Stage Meter-Range Prototype and Experiments

The superior properties of the proposed DFRs are demonstrated based on the abovementioned tests. In order to match the application of 110 kV high voltage post insulators, a prototype of the three-stage IPT system with a 1.54 m total length is built, as shown in Fig. 20.

The system prototype is built according to Figs. 12 and 14. The system is divided into primary stage, relay stage, and secondary stage. Among them, the length of each CSC is 0.18 m, and the length of the wireless gap between two adjacent stages is 0.5 m. In addition, four sets of DFRs whose parameters have been designed are placed among the wireless gaps.

The parameters of the abovementioned system prototype are shown in Table II. Among them, the parameters of the converter components can be obtained from the parameter manual. Measurement results of couplers and capacitors are obtained by impedance analyzer KEYSIGHT E4990A. Besides, after measuring the self-inductance and mutual inductance of each layer of the single-stage coupler, the equivalent decoupling inductance of each layer of each coupler is calculated by (6).

TABLE II
MAIN PARAMETERS UTILIZED IN THE PROTOTYPE

Parameter	Value/Type	Parameter	Value/Type
U_{in}	36/48/60 V	L_{R3}	1326.2 μH
f_0	100 kHz	C_{R1}	1.906 nF
$Q_1 - Q_4$	IRFBA22N50	C_{R2}	1.868 nF
$D_1 - D_4$	MBR40200WT	C_{R3}	1.910 nF
Ferrite Core	PC 40	R_R	2.70 Ω
R	20–200 Ω	L_{S1}	1225.3 μH
L_{P1}	1202.5 μH	L_{S2}	1243.0 μH
L_{P2}	1218.1 μH	L_{S3}	1212.6 μH
L_{P3}	1192.8 μH	C_{S1}	2.067 nF
C_{P1}	2.106 nF	C_{S2}	2.038 nF
C_{P2}	2.079 nF	C_{S3}	2.089 nF
C_{P3}	2.124 nF	R_S	2.44 Ω
R_P	2.35 Ω	M_{PR}	83.7 μH
L_{R1}	1328.7 μH	M_{RS}	84.5 μH
L_{R2}	1355.8 μH		

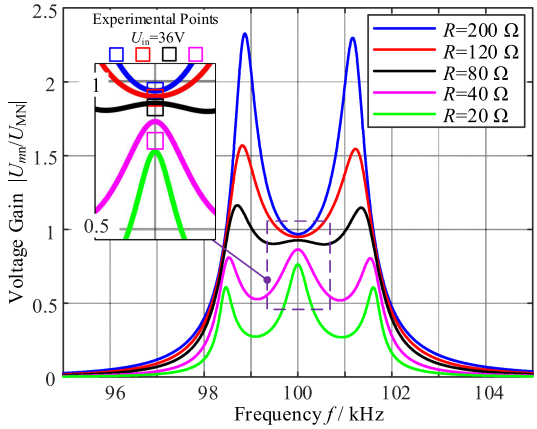

Fig. 21. Voltage gain curves of the three-stage meter-range IPT system.

The measured and initially calculated parameters were substituted into (7) and (8). The voltage gain equation of the IPT system is obtained by numerical analysis. Therefore, the frequency response curves of the system gain equation under different loads are obtained in Fig. 21.

In an ideal system, the gain value should be 1 at the resonant frequency. However, due to the existence of equivalent series resistance, the actual voltage gain value is relatively low. Among them, when the value of the load resistance is small, the decrease of the voltage gain is more severe due to the significant increase of the current. In addition, the comparison between the numerical analysis value and the measured value with 36 V input voltage is given in the right-side detailed figure at the resonant frequency.

In the following content, the characteristics of the proposed IPT system based on DFRs are verified by the designed experiments. Among them, the input voltages are, respectively, selected as standard dc voltages of 36 V, 48 V, and 60 V. Besides, the load varies from 20 to 200 Ω.

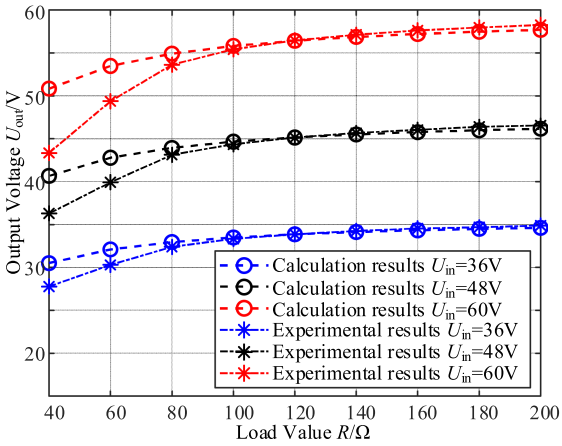

Fig. 22. Output voltage curves of the IPT system under experiments and calculations.

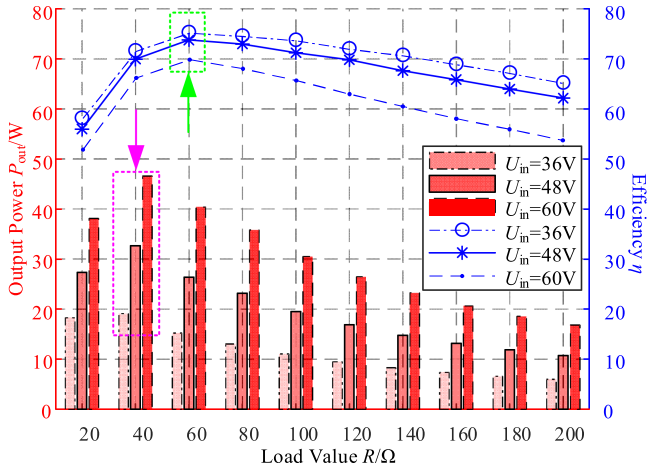

Fig. 23. Efficiency and output power of the IPT system.

The output voltage characteristics of the IPT system are obtained through experimental analysis, as shown in Fig. 22. The blue, black, and red star-shaped data points and curves in the figure represent the experimental results of output voltage with different input voltage. The corresponding circular points and lines represent the calculation results after the parameters in Table II are substituted into (10).

In Fig. 22, the trends of the experimental results and the calculated results are consistent, and the theoretical analysis is verified. Besides, the abovementioned trend of output voltage fluctuating with load changes shows that the voltage characteristics of the system have been obviously affected by large ESR. Among them, when the load resistance value is relatively low, the current flowing through the coil increases rapidly. Since the DFRs-based CSCs contain ferrite cores with nonlinear characteristics, the calculated results of the established numerical analysis linear model will deviate from the actual measured values. In addition, when the value of the load resistance increases to a certain extent, the IPT system approximately presents the characteristics of a voltage source constant voltage output.

The efficiency and output power of the IPT system are obtained through the experiments, and the results are shown in Fig. 23. The dotted curve shows the change trend of efficiency, and the histogram shows the situation of output power. Power and efficiency are distinguished in this figure by red and blue, which correspond to the vertical axes on the left and right sides, respectively.

According to the trend of the above experimental results in Fig. 23, the proposed IPT system based on DFRs can achieve the maximum efficiency at a load resistance value of 60 Ω and is circled with a green box. The maximum power can be output when the load resistance value is 40 Ω and is circled by the magenta box. Among them, when the input voltage is 36 V and the load resistance value is 60 Ω, the maximum efficiency of the system is 75.4%. In addition, when the input voltage is 60 V and the load resistance is 40 Ω, the maximum output power of the system is 46.6 W.

The maximum efficiency points at different input voltages are shown in Fig. 24. Among them, Fig. 24(a), (c), and (e) include

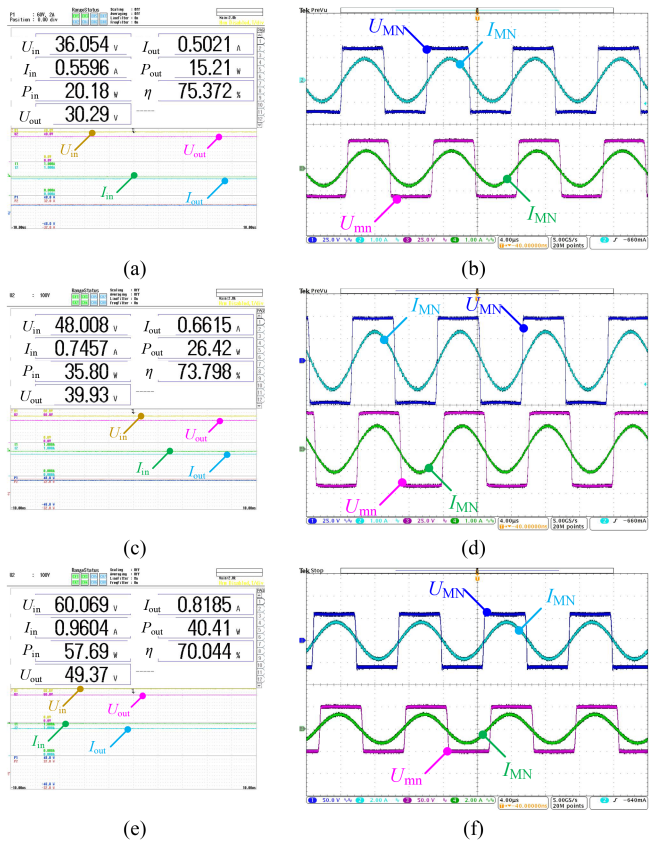

Fig. 24. Power, efficiency, and waveforms of the IPT system. (a) $U_{in} = 36$ V, $R = 60$ Ω, DC side. (b) $U_{in} = 36$ V, $R = 60$ Ω, AC side. (c) $U_{in} = 48$ V, $R = 60$ Ω, DC side. (d) $U_{in} = 48$ V, $R = 60$ Ω, AC side. (e) $U_{in} = 60$ V, $R = 60$ Ω, DC side. (f) $U_{in} = 60$ V, $R = 60$ Ω, AC side.

the waveforms and values of the dc side voltage, current, power of the input and output sides. The dc–dc efficiency of the IPT system is also included in Fig. 24(a), (c), and (e). In addition, the waveforms of the ac voltage and current at the input and output sides are shown in Fig. 24(b), (d), and (f).

The maximum efficiencies of the IPT system with a total wireless gap length of 1 m are all over 70% under three sets of

TABLE III
COMPARISON WITH SIMILAR WORKS IN RECENT YEARS

References	System Lenth	Efficiency	Power	Size of Each Coil	Stages	Details
This Work	1.54 m	75.4 % 70.0%	15.2 W 40.4 W	Φ 270 mm×180 mm	3	110 kV Post Insulator Application
2022[26]	1.54 m	59.5 %	8.05 W	Φ 230 mm×180 mm	3	110 kV Post Insulator Application
2022[25]	1.14 m	46%	20 W	Φ 198 mm×1.5 mm	13	PCB Resonators, 110 kV Composite Insulator
2022[23]	1.1 m	42.8%	2.1 W	Φ 140 mm×1.5 mm	12	Battery Charging, 110 kV Composite Insulator
2022[29]	0.2 m	75.4%	15.73 W	200×200×1.5 mm^3	6	PCB Resonators, Multiple loads, IGBT driver power supply
2021[27]	0.2 m	94%	12.6 W	150×150×5 mm^3	7	Multiple loads, IGBT driver power supply
2020[24]	1.14 m	11 %	6 W	Φ 200mm×1.6 mm	13	PCB Resonators, 110 kV Composite Insulator
2020[28]	0.4 m	83%	50 W	Φ 150mm×1.9 mm	5	Multiple loads, CC/CV switching
2019[21]	1.5 m	15 %	16.7 W	Φ 400 mm×50.4 mm	2	110 kV Insulation String Application

(a) (b) (c)

Fig. 25. Power, efficiency, and waveforms on DC side of the IPT system. (a) $U_{in} = 36$ V, $R = 40\ \Omega$. (b) $U_{in} = 48$ V, $R = 40\ \Omega$. (c) $U_{in} = 60$ V, $R = 40\ \Omega$.

input voltages, as shown in Fig. 24(a), (c), and (e). In addition, the waveforms of dc voltage and current are both horizontal straight lines without fluctuations. In Fig. 24(b), (d), and (f), the ac voltage is a square wave, and the ac current is a sine wave, which is not affected by harmonics. In addition, the phases of the input voltage and current waveforms are the same, indicating that the system is in a state of zero input phase angle at this time, and the inductance and capacitance elements are matched to resonance states.

The maximum output power points at different input voltages are shown in Fig. 25. The figure includes the waveforms and values of the dc side voltage, current, power, and efficiency of the input and output sides.

As a voltage source type approximate constant voltage output IPT system. According to the histogram trend in Fig. 23, it can be seen that the power will not continue to increase when the resistance value is further reduced from 40 Ω. Therefore, the output power can be further increased by increasing the input voltage if necessary.

Power transfer performances of the proposed IPT system with DFRs-based CSC are compared with similar works reported in recent years, as shown in Table III.

As a continuation of the previous work [26], the proposed DFRs significantly enhance the coupling coefficient between adjacent two stages of the domino cylindrical solenoid coupler and improve the self-inductance of each coil. Therefore, the efficiency of the IPT system is improved. Compared to the systems applied in composite insulators, the proposed IPT system employs much fewer stages and achieves higher efficiency. Compared to the systems with multiple loads for IGBT driver power supply applications, the proposed IPT system achieves a much longer power transfer distance.

Due to the reduction of the number of coils, the probability of failure of the Domino IPT system is drastically reduced, which provides the conditions for further extending the IPT distance by increasing the number of DFRs-based CSC stages.

V. CONCLUSION

A meter-range IPT system based on CSC with DFRs proposed in this article. The system is considered to be applied in 110 kV post insulators to power the state detection equipment for smart grids. The finite element analysis of the electric field is finished, and the insulating properties of the post insulators will not be affected with the inclusion of DFRs. The proposed DFRs can significantly reduce the reluctance of the CSC magnetic circuit, thereby increasing the coupling coefficient and inductance value so that the efficiency of the IPT system will be improved. The parameters of DFRs are optimized by finite element method to improve the performance of DFRs in terms of CSC inductance, mutual inductance, and coupling coefficient. A magnetic coupling structure based on multilayer cylindrical solenoid coils and DFRs is established. Decoupling distributed series compensation method and parameter calculation method are analyzed. A prototype of the system with 1.54 m total length to simulate 110 kV post insulator is built. The maximum efficiency of the IPT system with a total wireless gap of 1 m can reach 75.4%, and the efficiency can still reach 70% when the output power is 40.4 W. Compared with the previous similar works, the efficiency of the IPT system is significantly improved.

REFERENCES

[1] T. Kan, R. Mai, P. P. Mercier, and C. C. Mi, "Design and analysis of a three-phase wireless charging system for lightweight autonomous underwater vehicles," *IEEE Trans. Power Electron.*, vol. 33, no. 8, pp. 6622–6632, Aug. 2018.

[2] C. Cai, S. Wu, L. Jiang, Z. Zhang, and S. Yang, "A 500-W wireless charging system with lightweight pick-up for unmanned aerial vehicles," *IEEE Trans. Power Electron.*, vol. 35, no. 8, pp. 7721–7724, Aug. 2020.

[3] C. Jiang, K. T. Chau, W. Liu, C. Liu, W. Han, and W. H. Lam, "An LCC-compensated multiple-frequency wireless motor system," *IEEE Trans. Ind. Inform.*, vol. 15, no. 11, pp. 6023–6034, Nov. 2019.

[4] Q. Deng et al., "Wired/wireless hybrid charging system for electrical vehicles with minimum rated power requirement for DC module," *IEEE Trans. Veh. Technol.*, vol. 69, no. 10, pp. 10889–10898, Oct. 2020.
[5] C. Zhang, D. Lin, N. Tang, and S. Y. R. Hui, "A novel electric insulation string structure with high-voltage insulation and wireless power transfer capabilities," *IEEE Trans. Power Electron.*, vol. 33, no. 1, pp. 87–96, Jan. 2018.
[6] Y. Zhang, Z. Zhao, and K. Chen, "Frequency decrease analysis of resonant wireless power transfer," *IEEE Trans. Power Electron.*, vol. 29, no. 3, pp. 1058–1063, Mar. 2014.
[7] Y. Liu, W. Zhang, Y. Sun, M. Su, G. Xu, and H. Dan, "Review and comparison of control strategies in active power decoupling," *IEEE Trans. Power Electron.*, vol. 36, no. 12, pp. 14436–14455, Dec. 2021.
[8] Z. Zhang, H. Pang, A. Georgiadis, and C. Cecati, " Wireless power transfer—An overview," *IEEE Trans. Ind. Electron.*, vol. 66, no. 2, pp. 1044–1058, Feb. 2019.
[9] Q. Deng et al., "Frequency-dependent resistance of litz-wire square solenoid coils and quality factor optimization for wireless power transfer," *IEEE Trans. Ind. Electron.*, vol. 63, no. 5, pp. 2825–2837, May 2016.
[10] D. Liu and S. V. Georgakopoulos, "Cylindrical misalignment insensitive wireless power transfer systems," *IEEE Trans. Power Electron.*, vol. 33, no. 11, pp. 9331–9343, Nov. 2018.
[11] G. Zulauf and J. M. Rivas-Davila, "Single-turn air-core coils for high-frequency inductive wireless power transfer," *IEEE Trans. Power Electron.*, vol. 35, no. 3, pp. 2917–2932, Mar. 2020.
[12] C. Park, S. Lee, G.-H. Cho, and C. T. Rim, "Innovative 5-m-off-distance inductive power transfer systems with optimally shaped dipole coils," *IEEE Trans. Power Electron.*, vol. 30, no. 2, pp. 817–827, Feb. 2015.
[13] B. H. Choi, V. X. Thai, E. S. Lee, J. H. Kim, and C. T. Rim, "Dipole-coil-based wide-range inductive power transfer systems for wireless sensors," *IEEE Trans. Ind. Electron.*, vol. 63, no. 5, pp. 3158–3167, May 2016.
[14] B. G. Choi, J. H. Kim, E. S. Lee, H. R. Kim, and C. T. Rim, "Optimal dipole-coil ampere-turns design for maximum power efficiency of IPT," *IEEE Trans. Power Electron.*, vol. 35, no. 7, pp. 7317–7327, Jul. 2020.
[15] M. Wang, J. Feng, Y. Shi, and M. Shen, "Demagnetization weakening and magnetic field concentration with ferrite core characterization for efficient wireless power transfer," *IEEE Trans. Ind. Electron.*, vol. 66, no. 3, pp. 1842–1851, Mar. 2019.
[16] S. Seo, H. Jo, and F. Bien, "Free arrangement wireless power transfer system with a ferrite transmission medium and geometry-based performance improvement," *IEEE Trans. Power Electron.*, vol. 35, no. 5, pp. 4518–4532, May 2020.
[17] Y. Wang, P. Gu, Y. Yao, and D. Xu, "Analysis and design of cubic magnetic coupler for high distance-to-diameter ratio IPT systems," *IEEE Trans. Ind. Electron.*, vol. 69, no. 1, pp. 409–419, Jan. 2022.
[18] C. K. Lee, W. X. Zhong, and S. Y. R. Hui, "Effects of magnetic coupling of nonadjacent resonators on wireless power domino-resonator systems," *IEEE Trans. Power Electron.*, vol. 27, no. 4, pp. 1905–1916, Apr. 2012.
[19] W. X. Zhong, C. K. Lee, and S. Y. Hui, "Wireless power domino-resonator systems with noncoaxial axes and circular structures," *IEEE Trans. Power Electron.*, vol. 27, no. 11, pp. 4750–4762, Nov. 2012.
[20] W. Zhong, C. K. Lee, and S. Y. R. Hui, "General analysis on the use of tesla's resonators in domino forms for wireless power transfer," *IEEE Trans. Ind. Electron.*, vol. 60, no. 1, pp. 261–270, Jan. 2013.
[21] C. Cai et al., "Resonant wireless charging system design for 110-kV high-voltage transmission line monitoring equipment," *IEEE Trans. Ind. Electron.*, vol. 66, no. 5, pp. 4118–4129, May 2019.
[22] C. Cai et al., "Improved coplanar couplers based WPT systems for adaptive energy harvesting on power towers," *IEEE Trans. Electromagn. Compat.*, vol. 63, no. 3, pp. 922–934, Jun. 2021.
[23] Z. Yan et al., "A monitoring equipment charging system for HVTL based on domino-resonator WPT with constant current or constant voltage output," *IEEE Trans. Power Electron.*, vol. 37, no. 3, pp. 3668–3680, Mar. 2022.
[24] J. Qu, L. He, N. Tang, and C.-K. Lee, "Wireless power transfer using domino-resonator for 110-kV power grid online monitoring equipment," *IEEE Trans. Power Electron.*, vol. 35, no. 11, pp. 11380–11390, Nov. 2020.
[25] Y. Fang, J. Qu, B. M. H. Pong, C. K. Lee, and R. S. Y. Hui, "Quasi-static modeling and optimization of two-layer PCB resonators in wireless power transfer systems for 110-kV power grid online monitoring equipment," *IEEE Trans. Ind. Electron.*, vol. 69, no. 2, pp. 1400–1410, Feb. 2022.
[26] P. Gu et al., "A three-stage-five-coil IPT system based on cylindrical solenoid coupler applied to state detection equipment of HV device," *IEEE Trans. Power Electron.*, vol. 37, no. 2, pp. 2382–2393, Feb. 2022.
[27] C. Cheng, Z. Zhou, W. Li, Z. Deng, and C. C. Mi, "A power relay system with multiple loads using asymmetrical coil design," *IEEE Trans. Ind. Electron.*, vol. 68, no. 2, pp. 1188–1196, Feb. 2021.
[28] X. Xie, C. Xie, and L. Li, "Wireless power transfer to multiple loads over a long distance with load-independent constant-current or constant-voltage output," *IEEE Trans. Transp. Electrific.*, vol. 6, no. 3, pp. 935–947, Sep. 2020.
[29] S. Zhao et al., "A 4 kV/120 a SiC solid-state DC circuit breaker powered by a load-independent IPT system," *IEEE Trans. Ind. Appl.*, vol. 58, no. 1, pp. 1115–1125, Jan./Feb. 2022.

Peng Gu (Member, IEEE) was born in Harbin, China. He received the B.S. degree from Huazhong University of Science and Technology (HUST), Wuhan, China, in 2015, the M.S. degree from China Electric Power Research Institute, Beijing, China, in 2018, and the Ph.D. degree from Harbin Institute of Technology (HIT), Harbin, China, in 2023, all in electrical engineering.

He has been a Lecturer with the Department of Electrical Engineering, College of Information Science and Engineering, Northeastern University (NEU), Shenyang, China, since 2023. He is also working as a Postdoctoral Fellow with NEU of China in control science and engineering. His current research interests include wireless power transfer, magnetic coupling structure design, virtual power plant, electromagnetic transient analysis, overvoltage and insulation coordination of EHV/UHV ac system, and dc–dc converter.

Dr. Gu was the recipient of the outstanding graduate award of HUST and the best dissertation award for the doctoral degree of HIT.

Dongsheng Yang (Senior Member, IEEE) received the B.S. degree in testing technology and instrumentation, the M.S. degree in power electronics and electric drives, and the Ph.D. degree in control theory and control engineering from Northeastern University, Shenyang, China, in 1999, 2004, and 2007, respectively.

He is currently a Professor with Northeastern University. He was supported by the Program for New Century Excellent Talents in University. He has authored or coauthored around 70 papers published in academic journals and conference proceedings, 3 monographs, and coinvented 80 patents. His current research interests include distributed generation, wireless power transfer, multienergy power system, and artificial intelligence-based fault diagnosis and protection.

Dr. Yang was a recipient of the Second Prize of National Science and Technology Progress.

Guangdi Li (Member, IEEE) received the B.E.E. degree in electrical engineering from the College of Information Science and Engineering, Northeastern University, Shenyang, China, in 2013, and the Ph.D. degree in power electronics and electric drive from the College of Electrical Engineering, Zhejiang University, in 2020.

He is currently a Lecturer with the College of College of Information Science and Engineering, Northeastern University, Shenyang, China. He has authored and coauthored more than 15 SCI or EI indexed papers. He is a member of IEEE PES Intelligent Grid and Emerging Technologies Satellite Committee – China. His current research interests include resonant dc–dc converters, renewable energy generation and its control technology.

Dr. Li was the recipient of the first prize of science and technology progress award of Chinese Association of Automation, the second prize of science and technology progress award of China Machinery Industry Federation. He is also an active reviewer of some peer reviewed journals and international conferences.

Bowen Zhou (Member, IEEE) received the B.Sc. and M.Sc. degrees from Wuhan University, Wuhan, China, in 2010 and 2012, respectively, and the Ph.D. degree from Queen's University Belfast, Belfast, U.K., in 2016, all in electrical engineering.

He was with the Department of Electrical Engineering, College of Information Science and Engineering, Northeastern University, Shenyang, China, in 2016. He is currently an Associate Professor with Northeastern University. He is also the vice dean of School of Future Technologies, Northeastern University. He is the PI of more than 15 government and industry sponsored projects, including NSFC and National Key R&D Program of China. He has published more than 70 SCI or EI indexed papers and holds 20 patents, 5 software, and 1 standard. In total, 4 papers that he authored or coauthored have won best paper awards including IEEE TCE. His research interests include power and energy system operation and control, vehicle to grid, virtual energy storage and demand response, renewable energy, and energy internet.

Dr. Zhou is a member of the Expert Committee of China Energy Society. He is also a Standing Director or Director of several IEEE PES China committees and subcommittees. He was as a Youth Editorial Board Member and Special Issue Guest Editors of several international and domestic journals, and the session chairs and TC/PC members for more than 10 IEEE, IET, CCDC international conferences. He was the recipient of 4 first awards of provincial level science and technology advances award, and 2 silver awards of the 48th Geneva Inventions.

Fang Wei (Member, IEEE) received the B.S. degree in linguistics and culture from Dalian University of Foreign Languages, Dalian, China, in 2004, and the M.S. degree equivalent in applied linguistics from Northeastern University, Shenyang, China, in 2007.

She is currently an Associate Professor with the Institute of Foreign Languages, China Medical University, Shenyang, China. Her current research interests include technical translation, cross-cultural study, and scientific paper writing.

Honglu Guan was born in Henan, China, in 1992. He received the B.S. degree from Huazhong University of Science and Technology, Wuhan, China, in 2015, and the Ph.D. degree from Zhejiang University, Hangzhou, China, in 2020, all in electrical engineering.

He is currently an Engineer with State Grid Henan Electric Power Research Institute, Zhengzhou, China. His research interests include plasma science, insulation material modification, transformer, and electromagnetic field.